

Article

Parametric Design and Shape Sensing of Geared Back Frame Shell Structure for Floating Cylindrical Reflector Antenna off the Coast

Mengmei Mei, He Huang * , Yugang Li * and Zhe Zheng 

School of Mechanics, Civil Engineering and Architecture, Northwestern Polytechnical University, Xi'an 710072, China; meimengmei@mail.nwpu.edu.cn (M.M.); zhengzhe2018@mail.nwpu.edu.cn (Z.Z.)

* Correspondence: hehuang0623@nwpu.edu.cn (H.H.); ygli@nwpu.edu.cn (Y.L.)

Abstract: At present, numerous reflector antennas have been constructed worldwide on land. However, there are few applications of reflector antennas directly set off the coast. To expand the application region of reflector antennas, a floating cylindrical reflector antenna (FCRA) driven by the moving mass was developed to implement the elevation angle adjustment. Firstly, the structure design is introduced in detail. The design parameters are stated and analyzed to obtain the kinematic relationship while considering the water surface constraint. Then, the effects of each variable on the rotation capacity and structural stability are discussed. Further, the feasibility of the elevation angle adjustment process is demonstrated by using a prototype model test and software simulation. Finally, the deformation analyses and shape sensing of the back frame are carried out on the basis of the inverse finite element method (iFEM). We concluded that this new structure is feasible and expected to sit off the coast. In addition, the iFEM algorithm with sub-region reconstruction was proved to be suitable for the shape sensing of the over-constrained FCRA during the angle adjustment process via several quasi-static sampling moments.

Keywords: floating antenna; geared back frame; moving mass; iFEM; deformation reconstruction



Citation: Mei, M.; Huang, H.; Li, Y.; Zheng, Z. Parametric Design and Shape Sensing of Geared Back Frame Shell Structure for Floating Cylindrical Reflector Antenna off the Coast. *Appl. Sci.* **2023**, *13*, 11602. <https://doi.org/10.3390/app132011602>

Academic Editor: Victor Giurgiutiu

Received: 7 September 2023

Revised: 11 October 2023

Accepted: 18 October 2023

Published: 23 October 2023



Copyright: © 2023 by the authors. Licensee MDPI, Basel, Switzerland. This article is an open access article distributed under the terms and conditions of the Creative Commons Attribution (CC BY) license (<https://creativecommons.org/licenses/by/4.0/>).

1. Introduction

Reflector antennas have been applied to satellite communication, remote sensing, and radio astronomy for decades [1–4]. Radio astronomy detection is mainly carried out with single-aperture radio telescopes or interference array antennas. The antenna array can be composed of various antennas such as parabolic cylindrical reflector antennas, parabolic reflector antennas, and dipole oscillator arrays. Among these antennas, the large parabolic cylindrical reflector antenna is favored by more and more researchers due to its unique advantages such as high gain, strong directivity, and multiple feeds [5]. Since the 1950s, many countries have built a number of typical cylindrical reflector antennas in succession, such as the Ooty Radio Telescope [6], the Molonglo Observatory Synthesis Telescope of Australia [7], and the Nagoya IPS Stations of Japan [8]. China has also proposed a specific experimental prototype of the parabolic cylindrical reflector antennas in the Tianlai Project [9]. Some scholars have carried out the structural design and mechanical analysis of these parabolic cylindrical reflector antennas [10]. In 2015, China built an antenna array for dark energy detection that consisted of three 45×15 m parabolic cylindrical reflector antennas and sixteen parabolic reflector antennas [11]. All of these illustrate that there are broad development and application prospects for parabolic cylindrical reflector antennas.

Parabolic cylindrical reflector antennas can be divided into fixed antennas and movable antennas according to different observation objects [12]. The feed of the movable antenna is fixed to the reflector surface through brackets. Then, the reflector surface is mounted on the pitch axis through the back frame structure. Generally, the weight of an antenna is roughly proportional to the square of the aperture for movable antennas [13]. In comparison with

the fixed antenna, the movable reflector antenna can observe more signal sources and track a single signal source for a longer time. With increasing demands of observation, the aperture of the antenna becomes larger, which is followed by some challenges in mechanical rotation [14–16], feed support [17], and structural weight [18]. Furthermore, excessive weight brings great challenges regarding the construction process and production cost. It also causes a negative impact on the service life of reflector antennas. For example, since the start of its observations in 2001, the azimuth track of the Green Bank Telescope (GBT) has presented a series of problems due to its heavy weight and insufficient design, including tangential slippage of the base and wear plates, excessive tilting of the azimuth wheels, surface deterioration between the wear and base plates, fatigue fracture of bolts, cracks in wear plates, and so on [19–21].

Based on the background above, it has been stated that the huge weight of a large-aperture reflector is a critical challenge to the mechanical mechanism of movable antennas, which appeals to numerous scholars. Some scholars have committed to developing the design of mechanical systems and actively adjusting the reflector surface to improve the working performance [22–24]. Alternatively, some scholars have proposed some optimization ideas to reduce the weight and construction cost of reflector structures [25–27]. Most studies regard the movable reflector antenna on the ground. The gravity of the superstructure is concentrated on the azimuth mechanism, resulting in the range of problems mentioned above. In contrast, the movable reflector antenna set on the water surface can effectively resist the influence of gravity through buoyancy. Nevertheless, to the authors' knowledge, there are few studies on this [28].

Hence, a floating cylindrical reflector antenna (FCRA) is put forward in this study based on the current research. The buoyancy of water can resist the gravity of the structure. Then, the elevation angle of the reflector surface can be adjusted via the position change of the gravity center based on the moving mass inside the FCRA. The moving mass control has been studied on the roll control of flexible aircraft and the deformation control of flexible wings [29,30]. Hence, a moving mass gear drive method was adopted here to control the elevation angle adjustment for the reflector. There are several advantages of FCRA. The vast ocean space can be utilized to expand the sites of this movable reflector antenna. It can be combined with existing radio telescopes on land to form a very long baseline interferometry (VLBI) network. Furthermore, the size of a VLBI network can be extended to the scale of the Earth's diameter with the good mobility of an FCRA. Thus, a better observation performance can be obtained, and more signal sources can be tracked.

Further, in consideration of the effect of structural deformation on reflector accuracy, it is necessary to perform structural health monitoring (SHM) for the back frame structure of an FCRA. Known as shape sensing, the reconstruction of full-field structural deformation is a key component of SHM by utilizing discrete in situ strain measurements. Tessler and Spangler [31] developed a computationally efficient methodology called the inverse finite element method (iFEM) for the purpose of performing accurate shape sensing of plate and shell structures by using a three-node triangular inverse-shell element (iMIN3). The proposed method is based on a least-squares variational principle to reconstruct the full-field deformation from measured surface strains. Subsequently, more types of elements have been developed based on the work of Tessler, such as the four-node inverse-shell element (iQS4) [32] and the inverse beam–frame element [33]. Regarding the application of iFEM, it has been utilized in an offshore structure [34], a cantilever plate [35], a wing frame [36], a wind turbine tower [37], and so on. Numerous investigations have demonstrated the unique suitability of iFEM in terms of structural deformation monitoring. However, regarding the SHM of the back frame structure during the angle adjustment process, there is little research on the deformation reconstruction for the complex structure with over-constraints under a mechanism motion process.

In this paper, a new FCRA driven by a moving mass is developed using parametric design. The mechanism behaviors of this FCRA are analyzed via the mutual verification of the theoretical model, software simulation, and a prototype test. The shape sensing of

the back frame is carried out via iFEM methodology to reconstruct the three-dimensional displacement of the over-constrained structure during the angle adjustment process by using several quasi-static sampling moments. The paper is organized as follows. The structural design of the FCRA is introduced in Section 2. Then, the non-dimensional design parameters, kinematic relationship, water surface constraint, and structural stability are analyzed in Section 3. The elevation angle adjustment process is studied by using a prototype model test and software simulation in Section 4. Further, the iFEM algorithm based on the iQS4 element is briefly reviewed, and the deformation analysis and shape sensing for the back frame of the FCRA are carried out in Section 5. The conclusions are provided at the end of Section 6.

2. Structure Design

FCRA is composed of the reflector back frame and the trolley, as shown in Figure 1. The reflector back frame placed directly on the water surface is simplified to a semi-cylindrical shell with a circular arc track. The trolley with four gear wheels is connected to the track by the means of mutual gear meshing. The trolley rotates under the motor drive as a moving mass. Hence, FCRA is driven to realize the structure rotation and the elevation angle adjustment via the change in relative position between the back frame and the trolley. The track is directly fixed with the semi-cylindrical shell so as to improve the strength and stiffness of the back frame.

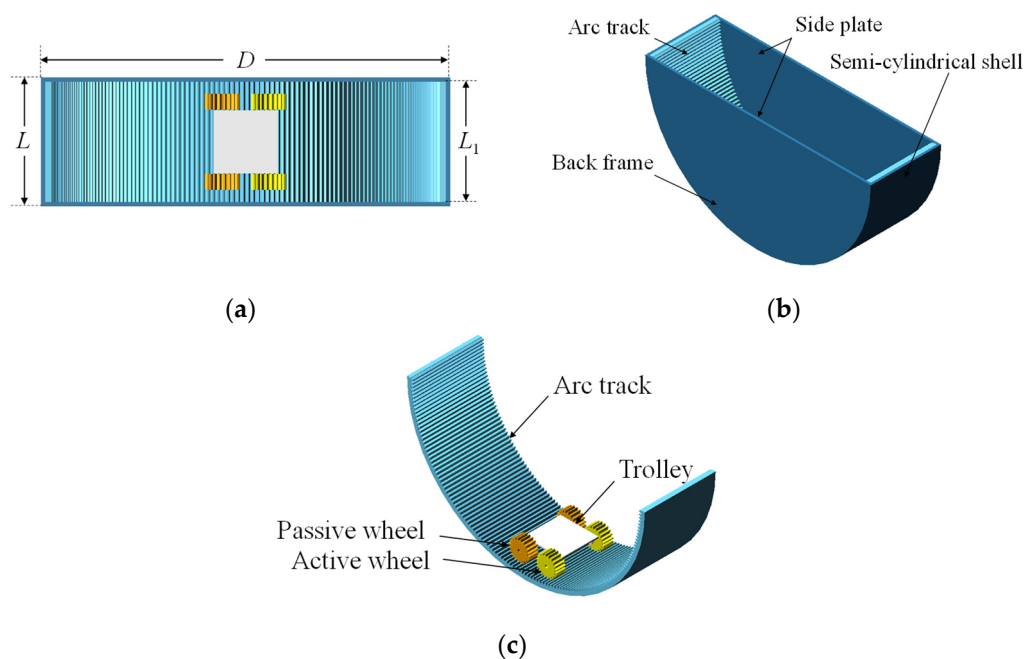


Figure 1. Structure design of FCRA. (a) Vertical view, (b) Axonometric view, (c) Axonometric view without semi-cylindrical shell.

Based on the structural design above, the transmission mechanism is one of the most important parts to fulfill the rotation for the FCRA. The internal ring gear meshing transmission mode is adopted here by parametric modeling as listed in Table 1. The gear model and the internal gear ring model are drawn by Pro-E in Figure 1.

It is worth mentioning that the modules of the gear and internal gear ring should be consistent to achieve the meshing transmission. The width of the circular arc track is 150 mm, referring to the internal gear ring in Table 1. Moreover, the back frame is covered with track. Thus, the design length along the longitudinal direction of the semi-cylindrical shell is approximately 150 mm.

Table 1. Design parameters of gear and ring.

Design Parameters	Gear	Internal Ring Gear	Unit
Module m	2	2	mm
Number of teeth z	20	240	\
Pitch diameter d	40	480	mm
Addendum circle diameter d_a	44	476	mm
Dedendum circle diameter d_f	35	485	mm
Base circle diameter d_b	44	451	mm
Tooth breadth b	20	150	mm
Pressure angle α	20	20	deg

3. Parameter Analyses

Some parameters are defined and analyzed to explore the relationship between the elevation angle adjustment and the trolley rotation. The influence of each variable on the rotation capacity and the structural stability of the FCRA is investigated below.

3.1. Parameter Definitions

The radius of the reflector surface is defined as R . The longitudinal length of the FCRA is L . The back frame shell thickness is t . The total track width is L_1 and the track thickness is t_1 . The density of water and the density of the back frame are ρ_w and ρ , respectively. The FCRA mass m is divided into several parts, which are side plate masses m_n , semi-cylindrical shell mass m_l , track masses m_t , and trolley mass m_s . The first three parts constitute the mass of the back frame, which is defined as $m_c = m_n + m_l + m_t$. These masses of each part in the back frame can be calculated as $m_n = \pi R^2 t \rho$, $m_l \approx \pi R t L \rho$, and $m_t \approx \pi R t_1 L_1 \rho$, respectively.

Assuming that the aperture D of the FCRA is 500 mm, the initial values of each design parameter are listed in Table 2 based on the model in Section 2, while reflector radius R and water density ρ_w are kept constant as their initial values. To easily study the effects of these parameters, the control variables are defined as the non-dimensional variables in Table 3.

Table 2. Initial values of design parameters.

Design Parameter	Value	Unit
Reflector aperture D	500	mm
Reflector radius R	250	mm
Longitudinal length L	150	mm
Shell thickness t	5	mm
Track width L_1	150	mm
Track thickness t_1	10	mm
Back frame density ρ	1.2×10^3	kg/m ³
Water density ρ_w	1.0×10^3	kg/m ³

Table 3. Ranges of non-dimensional control variables.

Control Variable	Initial Value	Range
$a = t/R$	0.02	[0.02, 0.10]
$b = L/R$	0.6	[0.4, 2.0]
$c = m_s/m$	0.3	[0.3, 1.0]
$n = \rho/\rho_w$	1.2	[1, 10]
$a_1 = t_1/R$	0.02	[0.02, 0.10]
$b_1 = L_1/R$	0.6	[0.4, 2.0]

3.2. Kinematic Relationship and Water Surface Constraint

The intersecting surface of the cylindrical paraboloid reflector is simplified into a parabola located in 2-dimensional Cartesian coordinate system XOY of Figure 2, the function of which is defined as $pz = x^2 + q$. It is assumed that the origin O is set up at the

circle center of the semi-cylindrical shell. The Z axis is perpendicular to this plane by the right-hand rule. The trolley is simplified as a moving mass.

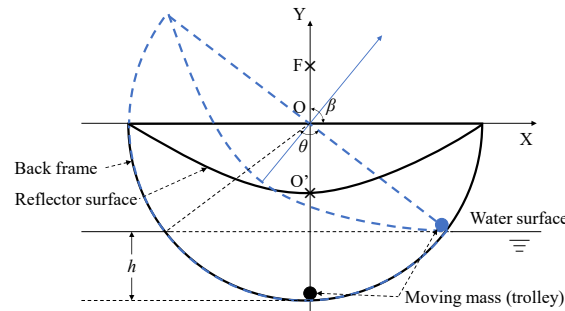


Figure 2. Parameter definitions (upright state of FCRA).

Since the FCRA is placed directly on the water, the immersion depth h into the water's surface is expressed by the central angle θ of the arc under the water's surface (Figure 2) as

$$h = R \left(1 - \cos \frac{\theta}{2} \right) \tag{1}$$

As simplified in the XOY plane, the reflector motion is indicated by the elevation angle β between the focal diameter O'F and axis X, where points O' and F are the vertex and focus of the reflect parabola, respectively, in Figure 2. The trolley is located at the center of the track while the focal diameter O'F of the reflector in the upright state coincides with axis Y of the global coordinate system in Figure 2.

To declare the relationship between the moving mass position and the reflector elevation angle, the FCRA motion process only considering the rigid body kinematics is divided into two stages as shown in Figure 3, namely moving mass motion and structure rotation.

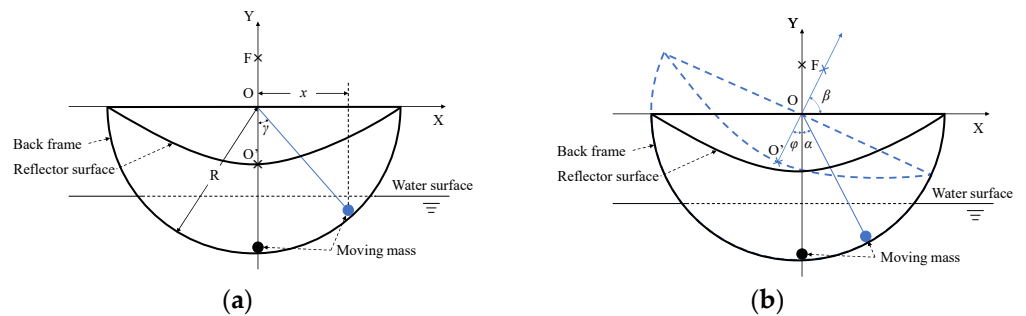


Figure 3. Moving mass motion and structural rotation. (a) Stage 1, mass moving relative to the track, (b) Stage 2, structure rotation.

Assuming that the back frame structure is immobile at the first stage in Figure 3a, only the motion of moving mass relative to the track is taken into account. The relative motion angle between the moving mass and the track is defined as γ .

At the second stage, the back frame structure is released to rotate around the central axis until there is an equilibrium for the whole structure. The elevation angle β of the reflector and the position of the moving mass are shown in Figure 3b. There is a torque equilibrium equation as $m_c R_c \sin \varphi = m_s R_s \sin \alpha$. Substituting the non-dimensional variables, it is expressed as Appendix A Equation (A1), where φ is the angle between axis Y and the focus diameter O'F in the equilibrium. α is the angle between the equilibrium position and initial position of the moving mass. The left and the right terms are the torque generated by the gravity of the back frame and the moving mass, respectively. The back frame centroid position R_c along the radial is written as Appendix A Equation (A2). In accordance with the geometric relationship in Figure 3, relative motion angle γ and the elevation angle β have relationships with the rotation angle φ and α as $\alpha + \varphi = \gamma$ and $\beta + \varphi = 90^\circ$. Then, the torque

equilibrium equation can be rewritten as Appendix A Equation (A3). Then, the elevation angle β is expressed as

$$\tan \beta = \frac{2(1 - c)(2a + 3ab + 3a_1b_1)}{3\pi c(a + ab + a_1b_1) \sin \gamma} + \frac{1}{\tan \gamma} \tag{2}$$

According to the expression $\beta = 90^\circ - \varphi$, the reflector in the upright state of $\beta = 90^\circ$ becomes horizontal along with the enlargement of φ and the reduction of β . Therefore, the upper-limit β_{\max} is 90° while the lower-limit β_{\min} depends on the rotation angle φ of the FCRA.

The rotation capacity is directly limited by the immersion depth h of the FCRA into the water's surface as shown in Figures 2 and 3b. This critical state of rotation capacity φ is determined as the position (Figure 2) of the back frame end reaching the water's surface. It means that this β_{\min} is equal to the half central angle of the arc under the water's surface, namely $\theta/2$. According to the Archimedes principle, the relationship between the gravity of the FCRA and the volume of water discharge can be written as $mg = \rho_w g Vd = \rho_w g LR^2(\theta - \sin\theta)/2$. It is expressed by non-dimensional variables as shown in Appendix A Equation (A4). Substituting β_{\min} into Appendix A Equation (A4), it can be reduced as

$$\beta_{\min} - \sin \beta_{\min} \cos \beta_{\min} = \frac{n\pi(a + ab + a_1b_1)}{b(1 - c)} \tag{3}$$

Particularly, the smaller total weight m becomes, the smaller lower-limit β_{\min} and the larger rotation capacity φ of the FCRA can achieve.

In addition, the rotation capacity meets the kinematic relationship between reflector elevation angle adjustment and moving mass rotation, namely Equation (2). Since the reflector elevation angle β turns into the lower-limit β_{\min} under the constraint of Equation (3), the relative motion angle γ becomes larger based on Equation (2). In general, the lower-limit β_{\min} represents the rotation capacity of the FCRA. The lower β_{\min} becomes, the larger the rotation capacity and elevation angle adjustment range, which means that the observation signal range of the FCRA is wider.

3.3. Structural Stability

Considering that the FCRA is located on water like ships [38,39], the structural stability should be guaranteed to avoid capsizing. Herein, only the transverse stability and initial stability are investigated with respect to the structural characteristics and working requirements. Assuming that a small heel angle δ occurs as shown in Figure 4, G, B, and B_1 are the centers of gravity, buoyancy without heeling, and buoyancy with a slight heeling angle. According to the position of G and B_1 , it can be seen that the condition $GB\sin\delta < BB_1$ can return the equilibrium under its own restoration moment after the heeling.

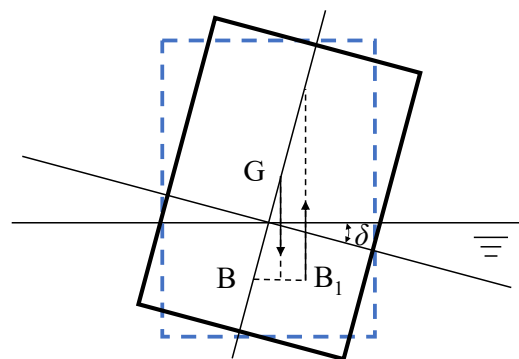


Figure 4. Left view before and after heeling.

Before the FCRA heels, combining with Appendix A Equation (A4), the distance between the center of gravity and the initial floating center is calculated as Appendix A

Equation (A5). It should be mentioned that the position of G may be lower than the position of B when the mass of the trolley accounts for a large proportion of the mass of the FCRA. In this case, Appendix A Equation (A5) is still valid for the stability of the FCRA.

After the FCRA has a slight heeling, in accordance with the principle of the center of gravity movement and Appendix A Equation (A4), the distance of the floating center movement can be written as Appendix A Equation (A6). Then, the condition to ensure the FCRA is restored to the horizontal floating state with the heeling angle δ can be described as Appendix A Equation (A7). It can be approximated that $\cos\delta \approx 1$. Then, the stability parameter S is defined as

$$S = b^3 - 4b \sin^3 \frac{\theta}{2} + 4n(2a + 3ab + 3a_1b_1) + 6n\pi(a + ab + a_1b_1) \frac{c}{1-c} > 0 \quad (4)$$

Hence, the stability of the FCRA increases with the increase in the value of S , which indicates the restorability of the FCRA when a small heeling occurs.

3.4. Parameter Study

The initial values of each design parameter and corresponding non-dimensional variable are kept the same as listed in Tables 2 and 3. The ranges of these non-dimensional control variables are consistent with the range in Table 3.

To investigate the relationship of these variables with the lower-limit β_{\min} and the stability parameter S , univariate curves of each non-dimensional parameter are drawn in Figure 5 based on Equations (3) and (4) while the rest of the variables are constants listed in Table 3.

In Figure 5, it is obvious that only the variable b corresponding to longitudinal length has a negative correlation with the lower-limit β_{\min} , and the other variables are positively correlated with the lower-limit β_{\min} . By selecting reasonable values of these parameters, the lower-limit β_{\min} can be controlled below 50° so that the rotation range is about 0° to 40° . Comparing the change in the lower-limit β_{\min} in Figure 5, it can be seen that shell thickness a , the ratio of the trolley mass to FCRA mass c , and back frame density n have great influence on the lower-limit β_{\min} with the differences as high as 40° , while the influence range of the others is somewhat small. Figure 5a,e represent that the effect of shell thickness a on the lower-limit β_{\min} is greater than track thickness a_1 when a and a_1 are in the same range. Longitudinal length b has a greater influence on the lower-limit β_{\min} than total track width b_1 as illustrated in Figure 5b,f. Additionally, the lower-limit β_{\min} becomes better with the increase in longitudinal length b while the lower-limit β_{\min} becomes worse with the increase in total track width b_1 .

There is positive correlation between these parameters and stability parameter S except the ratio of the trolley mass to FCRA mass c in Figure 5. There is transition in the curve of c and S as illustrated in Figure 5c. The corresponding value of S in the transition phase is below zero, which means that the value of c cannot meet the stability requirements (refer to Equation (4)). In addition, the value of c in the ascending phase is invalid as the value of β_{\min} cannot exceed 90° . In Figure 5, longitudinal length b and back frame density n have great influence on structural stability, followed by shell thickness a , the ratio of trolley mass to FCRA mass c , and total track width b_1 , and track thickness a_1 has the least influence on structural stability.

In summary, on the basis of ensuring the stability of the FCRA, the optimal parameter combination for obtaining the maximum rotation capacity of the FCRA is $a = 0.02$, $b = 2$, $c = 0.3$, $n = 1$, $a_1 = 0.02$, and $b_1 = 0.4$.

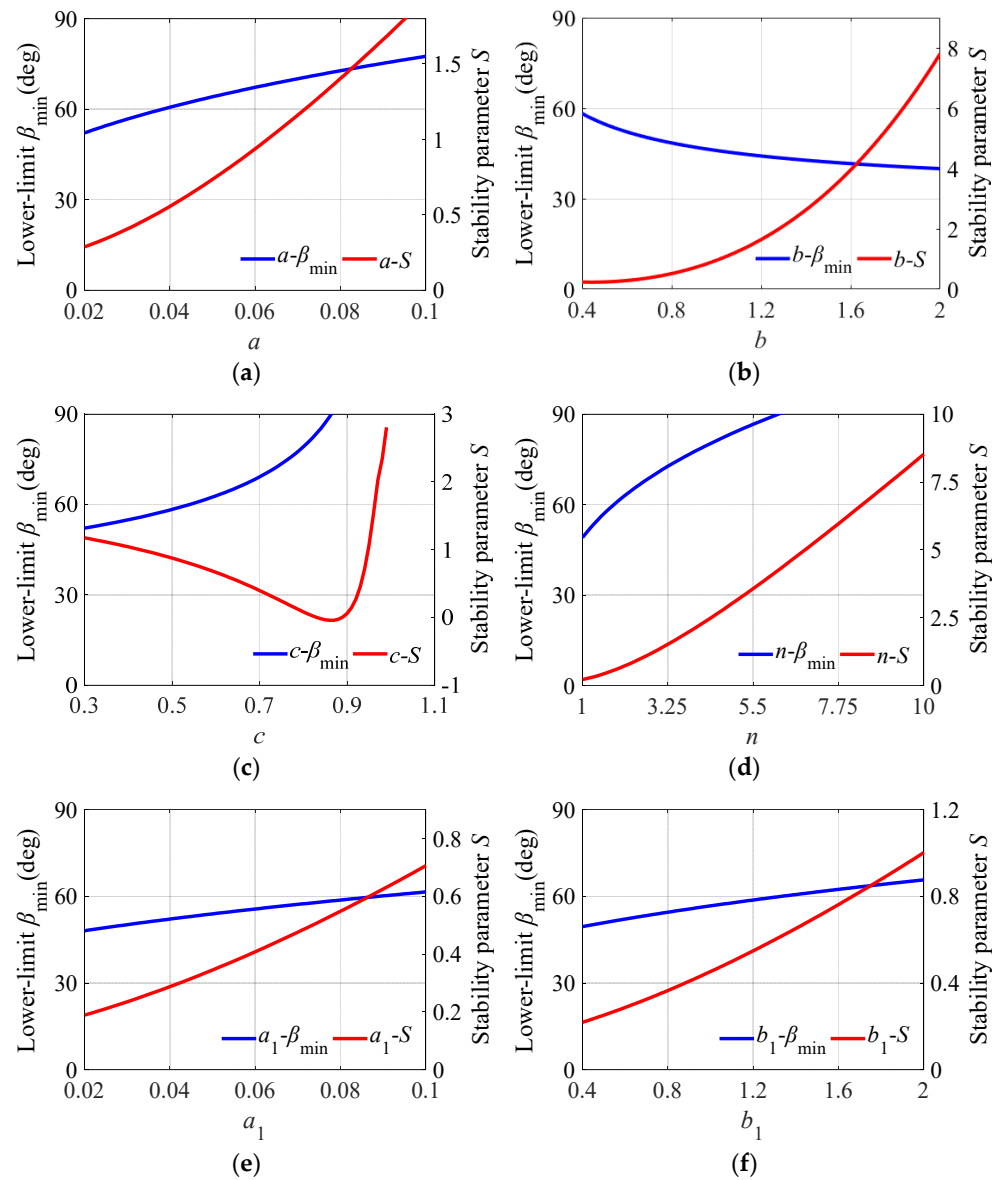


Figure 5. Parameter analyses. (a) Curves of $a - \beta_{\min}$ and $a - S$, (b) Curves of $b - \beta_{\min}$ and $b - S$, (c) Curves of $c - \beta_{\min}$ and $c - S$, (d) Curves of $n - \beta_{\min}$ and $n - S$, (e) Curves of $a_1 - \beta_{\min}$ and $a_1 - S$, (f) Curves of $b_1 - \beta_{\min}$ and $b_1 - S$.

4. Mechanism Analysis

The elevation angle adjustments of the FCRA are conducted by a prototype model test and software simulation to verify the rotation feasibility of the moving mass gear drive method.

4.1. Model of Analysis and Prototype

The prototype shown in Figure 6 is geometrically the same as the model in Section 3. The back frame is made of resin material whose density is $1.2 \times 10^3 \text{ kg/m}^3$. The four wheels of the trolley are made of steel and the density is $7.8 \times 10^3 \text{ kg/m}^3$. After adding load to the trolley, the masses of the trolley and back frame are 513.9 g and 292.3 g. The trolley is driven by the motor with wireless remote control. To easily observe the movement of the trolley and the rotation angle of the structure, the transparent side plates have a scale line every five degrees from the center along the radial direction. By measuring the size of each part for the prototype model, the actual initial values of each control variable in Table 3 are improved to $a = 0.024$, $b = 0.6$, $c = 0.637$, $n = 1.2$, $a_1 = 0.024$, and $b_1 = 0.6$.

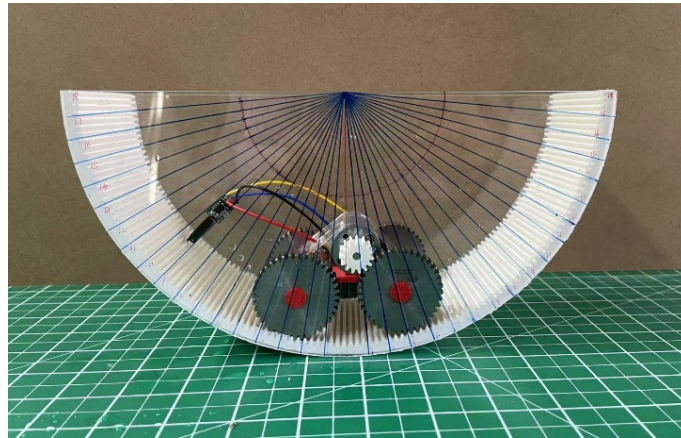


Figure 6. Prototype model.

The software Adams (MSC, Los Angeles, CA, USA, 2013) is employed here to study the elevation angle adjustment process of the FCRA. To match the prototype model test, the non-dimensional control parameters of the analysis model in ADMAS are kept consistent with the prototype model. To facilitate the display of internal structure, the shell is hidden in Figure 7b. The rotating pairs are arranged at the center of the back frame and the axles of the trolley. The same as the prototype model, the drive of the analysis model is applied to rotating pairs of back wheels. The contact friction is defined at the contact surfaces between the trolley and tracks. The tracks and the back frame shell are in a fixed form.

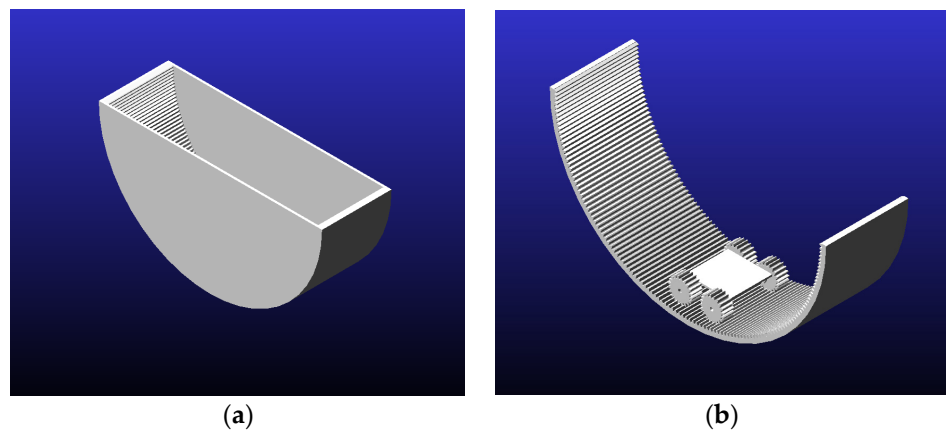


Figure 7. Analysis model. (a) Model in axonometric view, (b) Model without shell.

4.2. Rotation Process

The rotation process is one of the most important parts to verify the elevation angle adjustment for the FCRA. From the scale lines on the transparent side plate of the model, the relative motion angles γ of the trolley and the rotation angles φ of the back frame can be recorded. The elevation angle β can be further calculated according to $\beta + \varphi = 90^\circ$. The same relative motion angles γ in prototype tests are selected in the software simulation. These moments of rotation processes are listed in Figures 8 and 9. In order to observe the elevation angle and the position of the trolley better, the software simulation results are given in front view. Further, the kinematic relationships between γ and β based on the model test and software simulation are compared with the theoretical results from Equation (2) in Section 3. The error analysis for the three is listed Table 4.

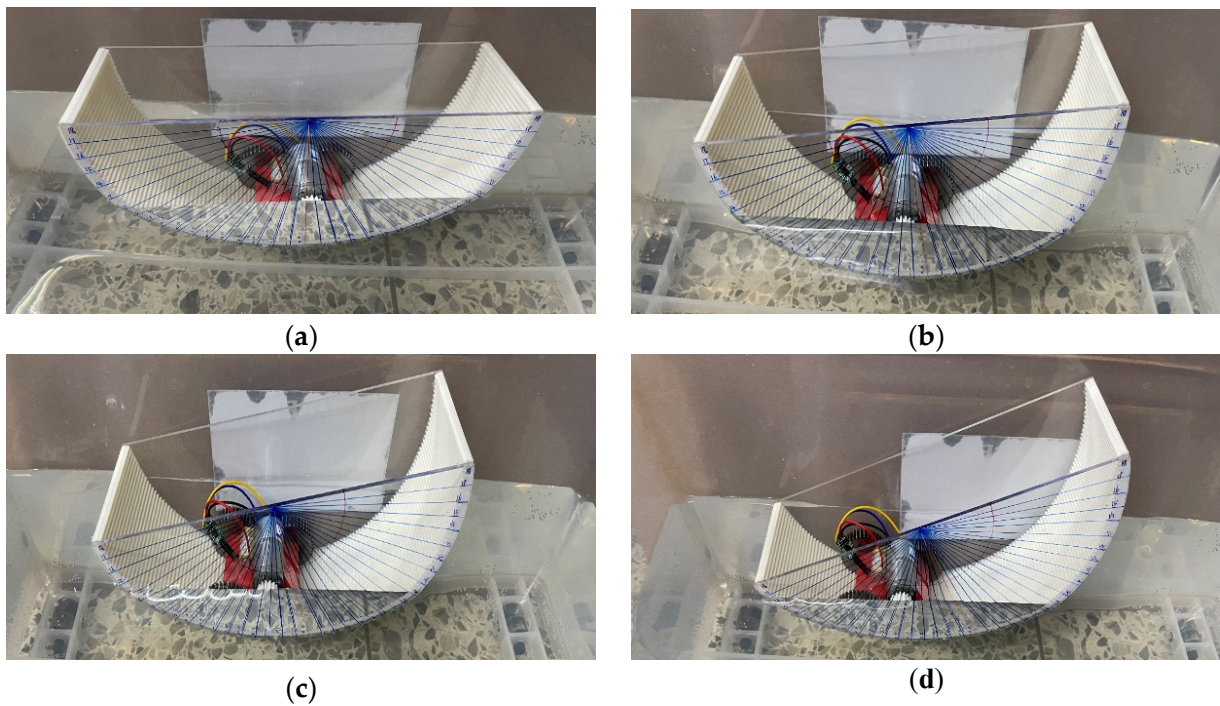


Figure 8. Rotation process of test. (a) $\gamma = 0^\circ$, $\beta = 90^\circ$, (b) $\gamma = 12.5^\circ$, $\beta = 80^\circ$, (c) $\gamma = 20^\circ$, $\beta = 75^\circ$, (d) $\gamma = 32.5^\circ$, $\beta = 65^\circ$.

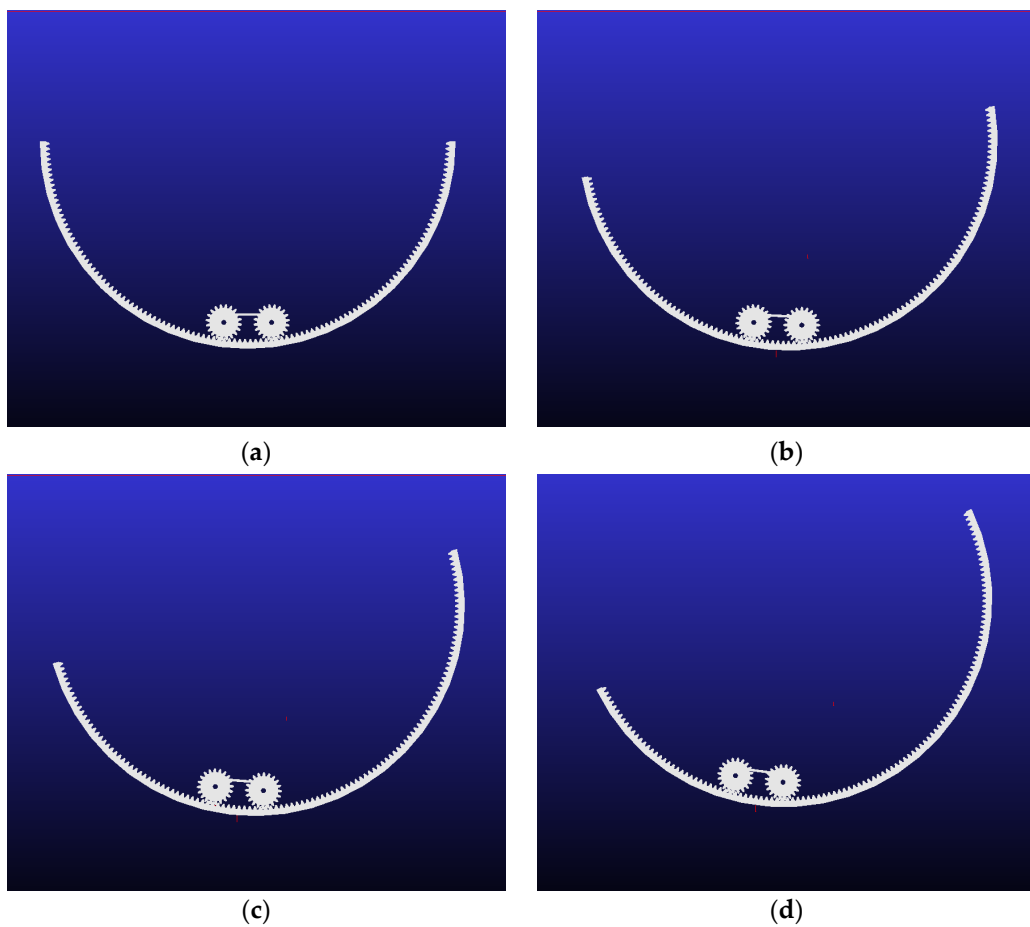


Figure 9. Rotation process of simulation. (a) $\gamma = 0^\circ$, $\beta = 90^\circ$, (b) $\gamma = 12.5^\circ$, $\beta = 80.13^\circ$, (c) $\gamma = 20^\circ$, $\beta = 74.21^\circ$, (d) $\gamma = 32.5^\circ$, $\beta = 64.18^\circ$.

Table 4. Error Analysis.

Central Angle γ	Elevation Angle β			Differences	
	Tests (a)	Simulation (b)	Theory (c)	a and c	b and c
0.0°	90°	90.00°	90.00°	0	0
12.5°	80°	80.13°	80.43°	0.53%	0.37%
20.0°	75°	74.21°	74.67°	0.44%	0.62%
32.5°	65°	64.18°	64.98°	0.03%	1.23%

From Figures 8 and 9, it is obvious that the results of software simulation match the rotation process of the model test well. In the model test, the central angle θ between the model and the water’s surface is 120° when the trolley is at the initial position. Since β_{\min} is equal to half of the central angle θ , the value of β_{\min} can be obtained as 60°. The lower-limit β_{\min} calculated by the water’s surface constraint is 63.6°. It is approximately 6% larger than the test result. It is inferred that the reasons for these differences have two parts. One part is about the manufacturing errors in the prototype model and the other is the numerical error of this theoretical solution to the transcendental equation Equation (3).

It can be seen from the differences in Table 4 that the errors between model test results and theoretical results are kept within 0.55%, indicating that the model test also matches theory well. The reason for the slight error may be because the scale line interval on the transparent side plate is so large that the reading accuracy is not high enough.

The error of the software simulation is larger than the error of the model test, which may be related to the contact setting between the trolley and the track in the software. Another reason is that the method of measurement in the model test is to wait for the trolley to reach a certain point until finding an equilibrium before reading the data, while the method of measurement in the software simulation involves real-time monitoring data. The structure is still in the motion state and does not reach the balance, which also results in a certain error. In general, compared with the results from Equation (2), the errors of the model test and software simulation are relatively small and within the acceptable range. It is indicated that the theory is correct and the moving mass gear drive method is feasible.

5. Deformation Analysis and Reconstruction

The deformation analyses of several specific rotation states corresponding to the rotation process of the prototype model test are carried out. The algorithm iFEM is performed for deformation reconstruction of the back frame.

5.1. Inverse Finite Element Method

The core of the iFEM algorithm is to construct an inverse element and construct the error functional between the analytical strain and measured strain based on the inverse element. The purpose of reconstructing the structural deformation is realized by finding the minimum value of the functional. Kefal et al. [32] developed a four-node inverse quadrilateral shell (iQS4) element which has six degrees of freedom (DOFs) per node as shown in Figure 10. Then, the element nodal displacement vector $\mathbf{u}^i = [u^i_1 \ u^i_2 \ u^i_3 \ u^i_4]^T$ can be expressed as $\mathbf{u}^i_q = [u_q \ v_q \ w_q \ \theta_{xq} \ \theta_{yq}]^T, (q = 1, 2, 3, 4)$.

According to the linear strain–displacement relations and the plane-stress assumption $\sigma_z = 0$ within the implication that the transverse-normal strain ϵ_{zz} does not contribute to the strain energy, the strain components can be combined to describe the membrane strain $\mathbf{e}(\mathbf{u}^i)$, bending curvatures $\mathbf{k}(\mathbf{u}^i)$, and transverse shear strain $\mathbf{g}(\mathbf{u}^i)$. Then, the strain–displacement relations are described as

$$[\epsilon_{xx} \ \epsilon_{yy} \ \gamma_{xy}]^T = \mathbf{e}(\mathbf{u}^i) + \mathbf{z}\mathbf{k}(\mathbf{u}^i)^i, [\gamma_{xz} \ \gamma_{yz}]^T = \mathbf{g}(\mathbf{u}^i) \tag{5}$$

The deformation reconstruction based on the iFEM algorithm requires the surface measurement strain data. Considering the discrete strain measurement method shown in Figure 11, the strain sensors are arranged on the top and bottom surfaces of the structure.

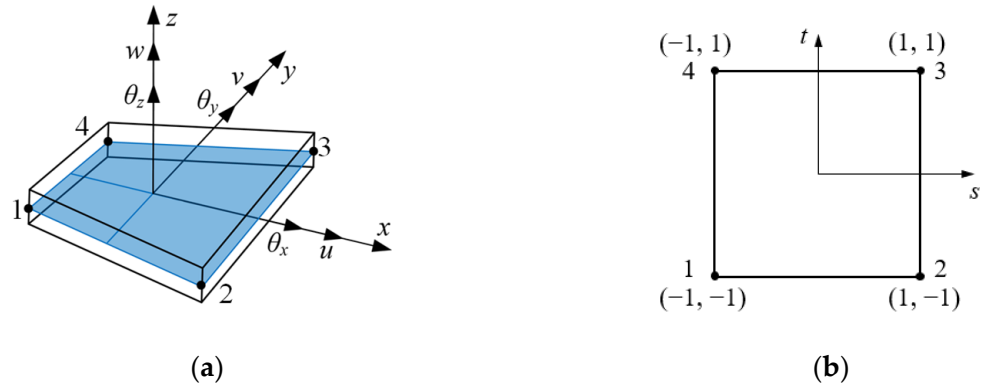


Figure 10. The four-node quadrilateral shell element (iQS4). (a) Element local coordinates, (b) Isoparametric coordinates.

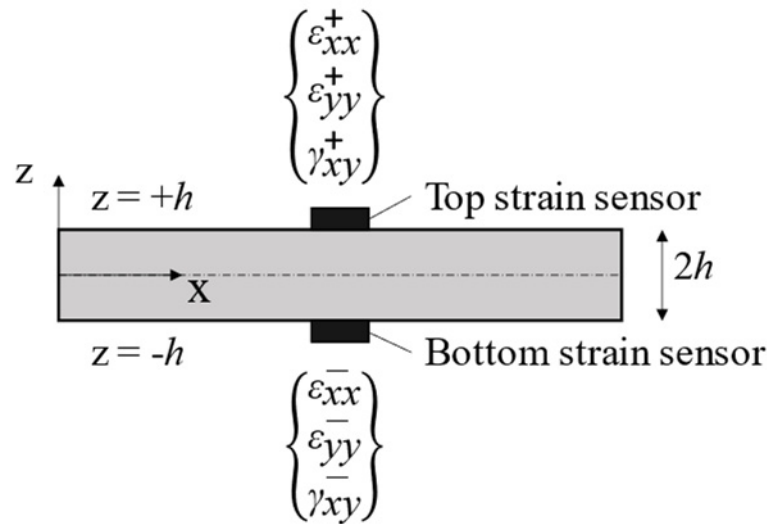


Figure 11. Discrete surface strain measurement.

The measured membrane strains e^ϵ and bending curvatures k^ϵ that correspond to their analytic counterparts $e(u^i)$ and $k(u^i)$ given by Equation (5) can be determined from the measured surface strain as

$$e^\epsilon = \frac{1}{2} \begin{Bmatrix} \epsilon_{xx}^+ + \epsilon_{xx}^- \\ \epsilon_{yy}^+ + \epsilon_{yy}^- \\ \gamma_{xy}^+ + \gamma_{xy}^- \end{Bmatrix}, \quad k^\epsilon = \frac{1}{2h} \begin{Bmatrix} \epsilon_{xx}^+ - \epsilon_{xx}^- \\ \epsilon_{yy}^+ - \epsilon_{yy}^- \\ \gamma_{xy}^+ - \gamma_{xy}^- \end{Bmatrix} \tag{6}$$

The key formulas of the iFEM algorithm are derived from the extreme value of the least-squares functional between the analytical strain in Equation (5) and measured strain in Equation (6). In terms of the iQS4 element, the functional takes the form as

$$\Phi(u^i) = w_m \|e(u^i) - e^\epsilon\|^2 + w_b \|k(u^i) - k^\epsilon\|^2 + w_s \|g(u^i) - g^\epsilon\|^2 \tag{7}$$

The unknown variable of the functional is the element nodal displacement vector \mathbf{u}^i . With regard to the variational principle and after some mathematical deduction, the condition for the minimum value of the function can be simply expressed as

$$\frac{\partial \Phi(\mathbf{u})}{\partial \mathbf{u}} = \mathbf{K}\mathbf{u} - \mathbf{F} = \mathbf{0} \quad (8)$$

Since the contribution of \mathbf{g}^ε is much smaller than \mathbf{e}^ε and \mathbf{k}^ε , it can be neglected in the calculation. With the nodal displacement vector transformed from the local coordinate to the global coordinate and the standard finite element integration operation, the element matrix of discrete structure is assembled into a linear equation. Furthermore, by imposing the displacement boundary conditions such that the matrix \mathbf{K} is non-singular, the iFEM equation can be solved to obtain the unique solution. Since the matrix \mathbf{K} only depends on the mesh discretization and the sensor distribution, it only needs to be calculated once. And the matrix \mathbf{F} is dependent on the measured strain values, thus, it needs to be updated at each time step during calculation.

5.2. Deformation Analyses

The aforementioned prototype model test has been analyzed and verified for the rigid body motion of the FCRA. Herein, the panels and shell of the back frame are taken for flexible deformation analysis. According to the physical size of the prototype model, the diameter of two side panels and the longitudinal length of the shell are 250 mm and 75 mm, and the thickness of the panels and shell is 3 mm. The material density of the back frame is $1.2 \times 10^3 \text{ kg/m}^3$ with an elastic modulus of 3.2 GPa and a Poisson's ratio of 0.35.

The three-dimensional finite element model of the back frame is established in ABAQUS (refer to Figure 12). To facilitate the mesh division and the application of boundary constraints, a small semi-circular hole is opened at the center of two side panels, and fixed constraints are placed at the hole. Considering the weight of the back frame, the weight of the trolley is equivalent to four concentrated forces applied at the contact point between the wheels and the tracks. The range of water pressure is calculated by Equation (1) and the hydrostatic pressure is applied to the outer surface of the back frame.

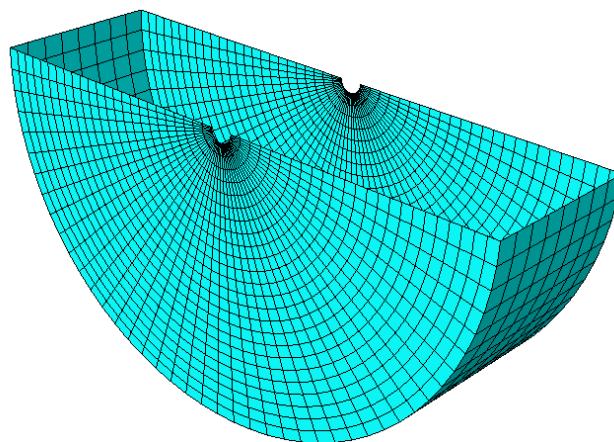


Figure 12. Finite element model of back frame.

To obtain accurate reference solutions, the high-fidelity mesh discretization in Figure 12 is performed with 2352 quadrilateral shell elements and 14,112 DOFs. The FEM analyses of the back frame at four rotational motion states recorded in Figures 8 and 9 are carried out as the quasi-static sampling moments for the following deformation reconstructions. The contours of total displacement for different rotation angles are presented in Figure 13.

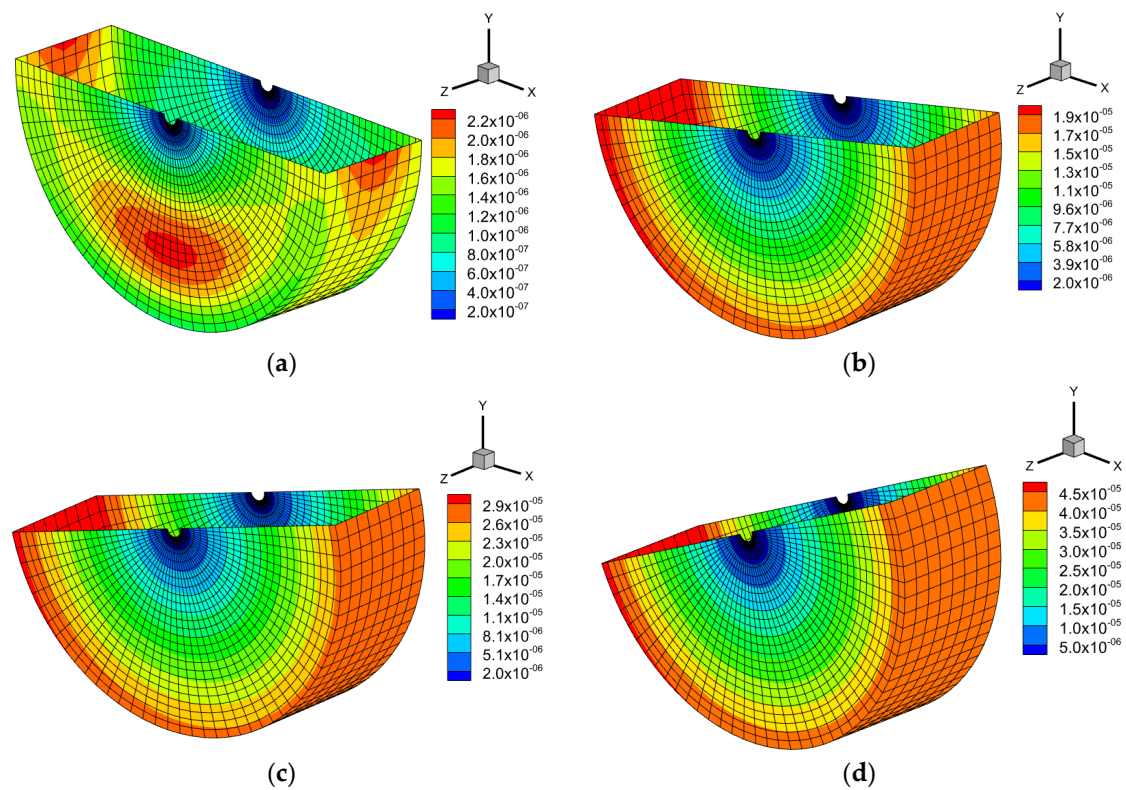


Figure 13. The FEM contours of total displacement in four rotation states. (a) $\beta = 90^\circ$, $\varphi = 0^\circ$, (b) $\beta = 80^\circ$, $\varphi = 10^\circ$, (c) $\beta = 75^\circ$, $\varphi = 15^\circ$, (d) $\beta = 65^\circ$, $\varphi = 25^\circ$.

From the results of deformation analysis in four different rotation states, the deformation of the panels and shell parts in the back frame becomes greater when the rotation angle φ of the FCRA becomes larger. Comparing the displacement deformation contour maps, only the deformation at $\varphi = 0^\circ$ shows a significant difference. The reason for this phenomenon may be that the positions of the concentrated force are not accurate enough, which leads to the rotation trend of the FCRA and some larger deformations in non-positive elevation states.

5.3. Deformation Reconstruction by iFEM

Due to the over-constraint of the back frame in a specific motion state, there may be discontinuous angular displacement at the connection between the panels and the shell. Exploiting the advantage of the iFEM algorithm that it does not need to consider the physical parameters such as external load during deformation reconstruction, the full-field deformation reconstruction of a statically indeterminate structure is realized by combining the sub-region division and iFEM algorithm. The reconstruction steps are as follows:

- (1) The measured discrete in situ strains in the iFEM algorithm are derived from the surface strains of FEM.
- (2) The back frame structure is divided into three sub-regions according to the boundary constraints, namely two side panels and a curved shell.
- (3) The iFEM algorithm is utilized to reconstruct the deformation of two side panels with fixed constraints.
- (4) The nodal displacements of two side panels at the joints are derived as the boundary constraints of the curved shell and input data in the iFEM code, then the deformation of the curved shell is reconstructed.
- (5) Integrating the reconstructed deformation of all sub-regions, the full-field deformation of the statically indeterminate structure is reconstructed.

The same mesh discretization as FEM and the above reconstruction steps are performed for the back frame structure. The measuring points are arranged at the center of each element and the discrete in situ strains in Figure 11 are derived from the strain results of FEM. The total displacement in four rotation states inverted by the iFEM algorithm are depicted in Figure 14. In addition, the inverse accuracy in four rotation states is demonstrated by the reference solution given by FEM, and the differences between iFEM results and FEM solutions are displayed in Table 5.

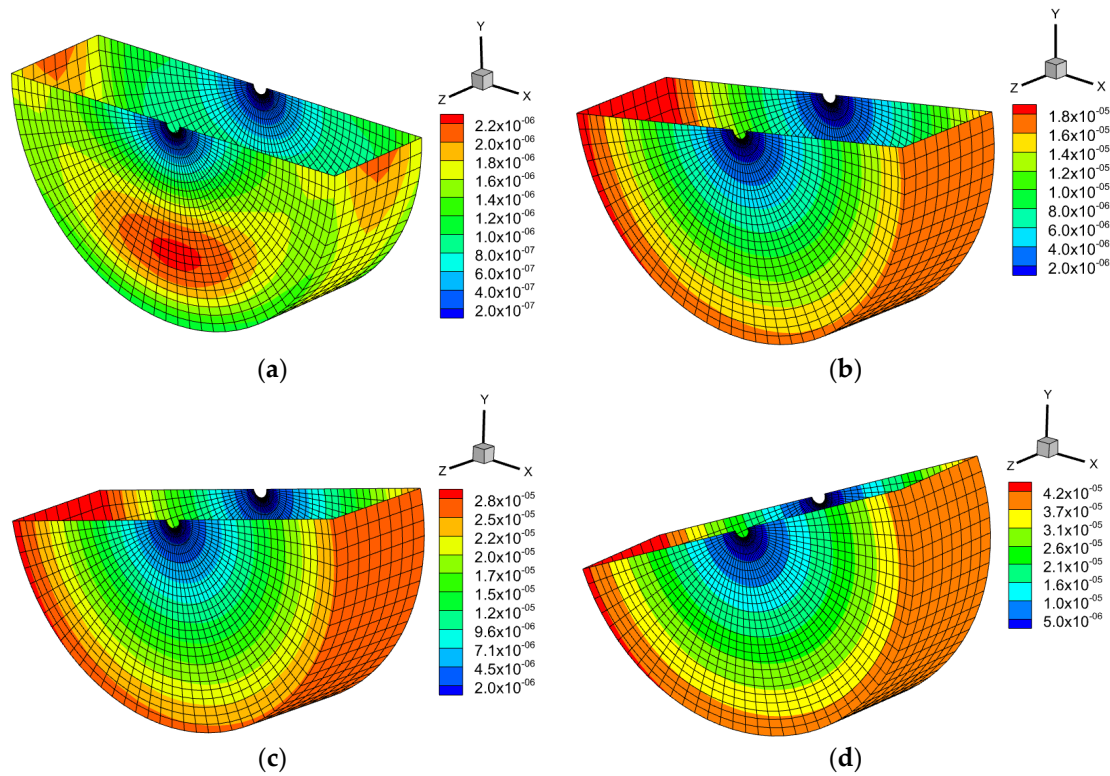


Figure 14. The iFEM contours of total displacement for fine mesh in four rotation states. (a) $\beta = 90^\circ$, $\varphi = 0^\circ$, (b) $\beta = 80^\circ$, $\varphi = 10^\circ$, (c) $\beta = 75^\circ$, $\varphi = 15^\circ$, (d) $\beta = 65^\circ$, $\varphi = 25^\circ$.

Table 5. Differences between iFEM and FEM results for different cases.

Elevation Angle β	Differences	Total Displacement	Total Rotation
65°	FEM and iFEM	5.55%	6.38%
75°	FEM and iFEM	5.08%	6.38%
80°	FEM and iFEM	4.15%	6.12%
90°	FEM and iFEM	1.31%	5.60%
90°	FEM and coarse iFEM	3.25%	6.41%

Further, another coarse mesh discretization method with 546 iQS4 elements and 3564 DOFs is adopted for the case at $\beta = 90^\circ$. The in situ strains of this inverse finite element (FE) model are also derived from the surface strains of FEM. Figure 15 displays the total displacement fields of the coarse inverse FE model. And the differences between iFEM results and FEM solutions are also listed in Table 5.

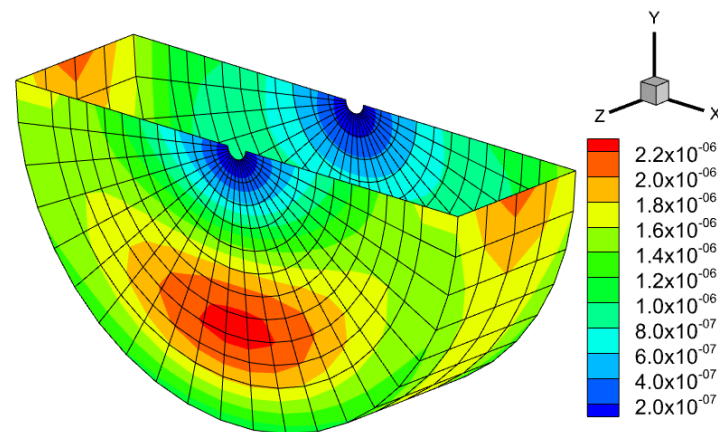


Figure 15. The iFEM contour of total displacement for coarse mesh at $\beta = 90^\circ$, $\varphi = 0^\circ$.

From Figures 13 and 14, it is clear that there is little difference between FEM solutions and iFEM reconstruction results. By comparing the deformation contours at $\beta = 90^\circ$ in Figures 13a, 14a, and 15, it is apparent that the full-field deformations reconstructed by two inverse FE models are highly consistent with the deformation calculated by FEM. With reference to the average reconstruction errors, the percentage errors of total rotation reconstruction are larger than that of total displacement reconstruction. With the increase in the rotation trend of the back frame, the reconstruction accuracy of the iFEM algorithm generally decreases to a certain degree. There are some greater errors of the inverse FE model in Figure 15 than in Figure 14 due to the coarser mesh of iQS4 elements. And it is indicated in Table 5 that the maximum relative percentage error of this coarse model is 6.41%, which appears in total rotation. Nevertheless, the average differences are available within the error range. These results suggest that the iFEM algorithm has an excellent shape-sensing performance for the back frame of the FCRA.

6. Conclusions

In this work, a floating cylindrical reflector antenna driven by a moving mass gear is developed to realize the elevation angle adjustment of the reflector surface. The specific structural design parameters are stated for the back frame structure of this FCRA while considering the kinematic relationship and water surface limitation. The effects of a single control variable on the elevation angle and the stability parameter are discussed, respectively. The prototype model test and software simulation are conducted to verify the feasibility of the moving mass gear drive method and the accuracy of parametric design. The deformation analyses for the back frame structure of the FCRA are carried out. And the iFEM algorithm with sub-region divisions is used for shape sensing of the over-constrained back frame structure during the angle adjustment process by four quasi-static sampling moments.

Based on the parametric analysis of the FCRA, the optimal parameter combination for the maximum rotation range is $a = 0.02$, $b = 2$, $c = 0.3$, $n = 1$, $a_1 = 0.02$, and $b_1 = 0.4$ while ensuring the stability of the FCRA. The errors in the rotation process between the theoretical calculation, software simulation, and prototype test are within 1.5%, which indicated that the parametric design is correct and the moving mass gear drive method is feasible. The deformation analysis of the back frame revealed that the total displacement increases with the growth of the rotation angle φ . The average differences in deformation reconstruction by iFEM are below 6.5%. It suggests that the iFEM algorithm with sub-regions is very suitable for the shape sensing of the over-constrained back frame structure. It is also confirmed that the iFEM algorithm by several quasi-static sampling can fulfill the deformation reconstruction with high precision during the rotation process.

Further work will focus on the influence of deformation on the reflector surface accuracy and technology development for the future applications of the FCRA.

Author Contributions: Conceptualization, H.H. and Y.L.; methodology, H.H. and M.M.; investigation, M.M. and Z.Z.; model analysis, M.M.; test, M.M. and Z.Z.; validation, Y.L.; writing—original draft preparation, M.M. and H.H.; writing—review and editing, H.H. and Y.L. All authors have read and agreed to the published version of the manuscript.

Funding: This work was supported by the National Natural Science Foundation of China (Grant No. 11902253 and 52278218), the Natural Science Foundation of Shaanxi Province, China (2021JM-065), and the Fundamental Research Funds for the Central Universities of China (310201906zy008).

Institutional Review Board Statement: Not applicable.

Informed Consent Statement: Not applicable.

Data Availability Statement: Data available on request due to restrictions, e.g., privacy or ethical.

Acknowledgments: The authors would like to thank the support of the aforementioned fund committees.

Conflicts of Interest: The authors declare that there are no conflict of interest. The funders had no role in the design of the study; in the collection, analyses, or interpretation of data; in the writing of the manuscript, or in the decision to publish the results.

Appendix A

Adopting the non-dimensional variables, the torque equilibrium equation can be expressed as

$$R_c \sin \varphi = \frac{c}{1-c} R \sin \alpha \tag{A1}$$

The back frame centroid position R_c along the radial is described as

$$R_c = \frac{\frac{4R}{3\pi} m_n + \frac{2R}{\pi} (m_l + m_t)}{m_c} = \frac{2(2a + 3ab + 3a_1 b_1)}{3\pi(a + ab + a_1 b_1)} R \tag{A2}$$

In accordance with the geometric relationship, relative motion angle γ and the elevation angle β have relationships with angle φ and α as $\alpha + \varphi = \gamma$ and $\beta + \varphi = 90^\circ$. Then, Equation (A1) can be rewritten as

$$\frac{2(2a + 3ab + 3a_1 b_1)}{3\pi(a + ab + a_1 b_1)} \cos \beta = \frac{c}{1-c} [-\cos(\gamma + \beta)] \tag{A3}$$

The relationship between the gravity of the FCRA and the volume of water discharge is expressed by non-dimensional variables as

$$\frac{(a + ab + a_1 b_1) n \pi R^3 \rho_w}{1-c} g = \frac{1}{2} b R^3 \rho_w g (\theta - \sin \theta) \tag{A4}$$

Combining with Equation (A4), the distance between the center of gravity and the initial floating center before the FCRA heels is calculated as

$$GB = \frac{2b(1-c) \sin^3 \frac{\theta}{2} - 2n(2a + 3ab + 3a_1 b_1)(1-c) - 3n\pi(a + ab + a_1 b_1)c}{3n\pi(a + ab + a_1 b_1)} R \tag{A5}$$

After the FCRA has a slight heeling, the distance of the floating center movement can be expressed as

$$BB_1 = \frac{b^3(1-c)}{6n\pi(a + ab + a_1 b_1)} R \tan \delta \tag{A6}$$

Then, the condition to ensure the FCRA is restored to the horizontal floating state after the heeling angle δ can be described as

$$\left[4b \sin^3 \frac{\theta}{2} - 4n(2a + 3ab + 3a_1 b_1) - 6n\pi(a + ab + a_1 b_1) \frac{c}{1-c} \right] \cos \delta - b^3 < 0 \tag{A7}$$

References

1. Rahmat-Samii, Y.; Haupt, R. Reflector Antenna Developments: A Perspective on the Past, Present and Future. *IEEE Antennas Propag. Mag.* **2015**, *57*, 85–95. [[CrossRef](#)]
2. Yao, G.; Xie, J.; Huang, W. HF Radar Ocean Surface Cross Section for the Case of Floating Platform Incorporating a Six-DOF Oscillation Motion Model. *IEEE J. Ocean. Eng.* **2021**, *46*, 156–171. [[CrossRef](#)]
3. Li, M.; Wu, X.; Chen, Z.; Liu, J.; Emery, W.J.; Li, C. A Scheme for Multitarget Lateral Velocity Measurement with High-Frequency Monostatic Radar. *IEEE J. Ocean. Eng.* **2020**, *45*, 1427–1438. [[CrossRef](#)]
4. Du, X.; Johnson, T.; Landecker, T.; Veidt, B. An Ultrawideband Nested Coaxial Waveguide Feed Antenna for Radio Astronomy. *IEEE Trans. Antennas Propag.* **2022**, *70*, 2499–2509. [[CrossRef](#)]
5. Sengupta, D.L. Parabolic Cylindrical Reflector Antennas. *IETE J. Res.* **2015**, *11*, 248–255. [[CrossRef](#)]
6. Subrahmanya, C.R.; Manoharan, P.K.; Chengalur, J.N. The Ooty Wide Field Array. *J. Astrophys. Astron.* **2017**, *38*, 10. [[CrossRef](#)]
7. Mills, B.Y.; Aitchison, R.E.; Little, A.G.; Mcadam, W.B. The Sydney University cross-type radio telescope. *Proc. IREE* **1963**, *24*, 1963.
8. Tokumaru, M. Three-dimensional exploration of the solar wind using observations of interplanetary scintillation. *Proc. Jpn. Acad.* **2013**, *89*, 67–79. [[CrossRef](#)] [[PubMed](#)]
9. Chen, X.L. Radio detection of dark energy—The Tianlai project. *Sci. Sin. Phys. Mech. Astron.* **2011**, *41*, 1358–1366. [[CrossRef](#)]
10. Zhu, J.L.; Chen, Z.P.; Zhang, J.Y.; Liu, R. Development of special test antenna for Tianlai project. *Electro-Mech. Eng.* **2014**, *30*, 32–36. [[CrossRef](#)]
11. Liu, C.; Shi, H.L.; Chen, X.L. A new space target detection technology and its experiment by using Tianlai Dark Energy radio detection array. *J. Astronaut* **2017**, *38*, 1243–1252.
12. Sun, Z.J. Design of Large Rotatable Cylinder Antenna Drive System. Master's Thesis, Hangzhou Dianzi University, Hangzhou, China, 2021.
13. Wu, Y.K. Structure Design and Simulation Analysis of Large Rotatable Parabolic Cylindrical Antenna. Master's Thesis, Hangzhou Dianzi University, Hangzhou, China, 2020.
14. Gawronski, W.; Baher, F.; Quintero, O. Azimuth-track level compensation to reduce blind-pointing errors of the deep space network antennas. *IEEE Antennas Propag. Mag.* **2000**, *42*, 28–38. [[CrossRef](#)]
15. Ling, Q.B.; Liu, W.M.; Fu, L.; Liu, G.X. Shanghai 65-m diameter radio telescope azimuth track mechanics analysis. *Ann. Shanghai Astron. Obs. Chin. Acad. Sci.* **2011**, *00*, 83–89.
16. Wang, W. Influence Mechanism of Mechanical Factors on Electrical Performance of Reflector Antenna and Its Applications. Ph.D. Thesis, Xidian University, Xi'an, China, 2011.
17. Chen, Z.P.; Wang, R.; Peterson, J.; Chen, X.L.; Zhang, J.; Shi, H. Design and analysis of a large cylinder antenna array in Tianlai. In Proceedings of the SPIE—The International Society for Optical Engineering, Edinburgh, UK, 26 June–1 July 2016.
18. Chen, Z.P.; Wu, Y.K.; Shi, H.L.; Shou, J.J.; Li, F.; Wang, Z.; Sun, Z.J. Research on Light-Weight Design and Simulation Analysis of Large Steerable Parabolic Cylindrical Antenna. In *Lecture Notes in Electrical Engineering*; Springer: Singapore, 2019.
19. Prestage, R.M.; Constantinescu, K.T.; Hunter, T.R.; King, L.J.; Lacasse, R.J.; Lockman, F.J.; Norrod, R.D. The green bank telescope. *Proc. IEEE* **2009**, *97*, 1382–1390. [[CrossRef](#)]
20. Symmes, A.; Anderson, R.; Egan, D. Improving the service life of the 100-meter green bank telescope azimuth track. In Proceedings of the SPIE—The International Society for Optical Engineering, Marseille, France, 23–28 June 2008. [[CrossRef](#)]
21. Anderson, R.; Symmes, A.; Egan, D. Replacement of the green bank telescope azimuth track. In Proceedings of the SPIE—The International Society for Optical Engineering, Marseille, France, 23–28 June 2008. [[CrossRef](#)]
22. Kaercher, H.J. Azimuth axis design for huge telescopes: An update. In Proceedings of the SPIE—The International Society for Optical Engineering, Glasgow, UK, 21–25 June 2004. [[CrossRef](#)]
23. Wang, C.-S.; Xiao, L.; Wang, W.; Xu, Q.; Xiang, B.-B.; Zhong, J.-F.; Jiang, L.; Bao, H.; Wang, N. An adjustment method for active reflector of large high-frequency antennas considering gain and boresight. *Res. Astron. Astrophys.* **2017**, *17*, 43. [[CrossRef](#)]
24. Wang, J.-Q.; Sun, Z.-X.; Fu, L.; Li, J.-L.; Yu, L.-F.; Jiang, Y.-C.; Gou, W.; Hu, W.; Zhao, R.-B.; Liu, Q.-H.; et al. Research on actuator distribution and panels for a radio telescope. *Res. Astron. Astrophys.* **2021**, *21*, 33–38. [[CrossRef](#)]
25. FENG, S.; DUAN, X.; DUAN, B. A novel design of large full-steerable reflector antenna. *Sci. Sin. Phys. Mech. Astron.* **2017**, *47*, 059509. [[CrossRef](#)]
26. Boonstra, A.; Nijboer, R. Radio Telescope Design Optimization Using Costing Constraints: Extrapolating LOFAR Costing to the Square Kilometre Array. *Radio Sci.* **2018**, *53*, 1346–1355. [[CrossRef](#)]
27. Zhang, S.; Song, J. Surface segmentation design using a weighting level set topology optimization method for large radio telescope antennas. *Struct. Multidiscip. Optim.* **2021**, *64*, 905–918. [[CrossRef](#)]
28. Loni, Z.M.; Espinosa, H.G.; Thiel, D.V. Floating Hemispherical Helical Antenna for Ocean Sensor Networks. *IEEE J. Ocean. Eng.* **2018**, *44*, 1041–1048. [[CrossRef](#)]
29. Wang, X.; Zhou, W.; Mu, R.; Wu, Z. Modeling and simulation of mass-actuated flexible aircraft for roll control. *Aerosp. Sci. Technol.* **2020**, *107*, 106254. [[CrossRef](#)]
30. Wang, X.; Zhou, W.; Mu, R.; Wu, Z. A new deformation control approach for flexible wings using moving masses. *Aerosp. Sci. Technol.* **2020**, *106*, 106118. [[CrossRef](#)]

31. Tessler, A.; Spangler, J.L. A least-squares variational method for full-field reconstruction of elastic deformations in shear-deformable plates and shells. *Comput. Methods Appl. Mech. Eng.* **2005**, *194*, 327–339. [[CrossRef](#)]
32. Kefal, A.; Oterkus, E.; Tessler, A.; Spangler, J.L. A quadrilateral inverse-shell element with drilling degrees of freedom for shape sensing and structural health monitoring. *Eng. Sci. Technol. Int. J.* **2016**, *19*, 1299–1313. [[CrossRef](#)]
33. Gherlone, M.; Cerracchio, P.; Mattone, M.; Di Sciuva, M.; Tessler, A. Shape sensing of 3D frame structures using an inverse Finite Element Method. *Int. J. Solids Struct.* **2012**, *49*, 3100–3112. [[CrossRef](#)]
34. Kefal, A.; Oterkus, E. Shape and stress sensing of offshore structures by using inverse finite element method. In Proceedings of the MARSTRUCT 2017, the 6th International Conference on Marine Structures, Lisbon, Portugal, 8–10 May 2017. [[CrossRef](#)]
35. Li, M.; Jia, D.; Wu, Z.; Qiu, S.; He, W. Structural damage identification using strain mode differences by the iFEM based on the convolutional neural network (CNN). *Mech. Syst. Signal Process.* **2022**, *165*, 108289. [[CrossRef](#)]
36. Zhao, Y.; Du, J.; Bao, H.; Xu, Q. Optimal Sensor Placement Based on Eigenvalues Analysis for Sensing Deformation of Wing Frame Using iFEM. *Sensors* **2018**, *18*, 2424. [[CrossRef](#)] [[PubMed](#)]
37. Li, M.; Kefal, A.; Oterkus, E.; Oterkus, S. Structural health monitoring of an offshore wind turbine tower using iFEM methodology. *Ocean Eng.* **2020**, *204*, 107291. [[CrossRef](#)]
38. Choi, J.-H.; Jensen, J.J. Extreme value predictions using FORM for ship roll motions. *Mar. Struct.* **2019**, *66*, 52–65. [[CrossRef](#)]
39. Grammatikopoulos, A. The effects of geometric detail on the vibratory responses of complex ship-like thin-walled structures. *Mar. Struct.* **2021**, *78*, 103013. [[CrossRef](#)]

Disclaimer/Publisher’s Note: The statements, opinions and data contained in all publications are solely those of the individual author(s) and contributor(s) and not of MDPI and/or the editor(s). MDPI and/or the editor(s) disclaim responsibility for any injury to people or property resulting from any ideas, methods, instructions or products referred to in the content.